Chemical Structure of Fe-Ni Nanoparticles for Efficient Oxygen Evolution Reaction (OER) Electrocatalysis

Prashant Acharya[ǂ], *Zachary J. Nelson*[ǂ], *Mourad Benamara*[§], *Ryan H. Manso*[¶], *Sergio I. Perez Bakovic*[ǂ], *Mojtaba Abolhassani*[ǂ], *Sungsik Lee*[◊], *Benjamin Reinhart*[◊], *Jingyi Chen*[¶], *and Lauren F. Greenlee*[*ǂ]

ǂ Ralph E. Martin Department of Chemical Engineering, University of Arkansas, Fayetteville, AR 72701

§ Institute for Nanoscience and Engineering, University of Arkansas, Fayetteville, AR 72701

¶ Department of Chemistry and Biochemistry, University of Arkansas, Fayetteville, AR 72701

◊ Advanced Photon Source, Argonne National Lab, Argonne, IL 60439

KEYWORDS: iron, nickel, oxygen evolution reaction, nanoparticles, catalysts, x-ray absorption spectroscopy, electrochemistry

ABSTRACT:

Bimetallic iron-nickel-based nanocatalysts are perhaps the most active for the oxygen evolution reaction (OER) in alkaline electrolyte. Recent developments in literature have suggested that the ratio of iron and nickel in Fe-Ni thin films plays an essential role in the performance and stability of the catalysts. In this work, the metallic ratio of iron to nickel was tested in alloy bimetallic nanoparticles. Similar to thin films, nanoparticles with iron-nickel atomic compositions where the atomic iron percentage is ≤ 50% outperformed nanoparticles with iron-nickel ratios of > 50%. Nanoparticles of $Fe_{20}Ni_{80}$, $Fe_{50}Ni_{50}$, and $Fe_{80}Ni_{20}$ compositions were evaluated and demonstrated to have overpotentials of 313 mV, 327 mV, and 364 mV, respectively, at a current density of 10 mA/cm^2. While the $Fe_{20}Ni_{80}$ composition might be considered to have the best OER performance at low current densities, $Fe_{50}Ni_{50}$ was found to have the best current density performance at higher current densities, making this composition particularly relevant for electrolysis conditions. However, when stability was evaluated through chronoamperometry and chronopotentiometry, the $Fe_{80}Ni_{20}$ composition resulted in the lowest degradation rates of 2.9 μA/hr and 17.2 μV/hr, respectively. These results suggest that nanoparticles with higher iron and lower nickel content, such as the $Fe_{80}Ni_{20}$ composition, should be still taken into consideration while optimizing these bimetallic OER catalysts for overall electrocatalytic performance. Characterization by electron microscopy, diffraction, and x-ray spectroscopy provides detailed chemical and structural information on as-synthesized nanoparticle materials.

1 INTRODUCTION

The global economy remains heavily reliant on fossil-fuel based non-renewable sources of energy.[1] Fossil fuels are a major contributor to greenhouse gases, as the burning of fossil fuels leads to the release of carbon dioxide (CO_2) in the atmosphere.[2] In 2013 alone, an estimated 9.78 billion metric tons of CO_2 were released into the atmosphere due to the use of fossil fuels.[3] Having fuel alternatives to fossil fuels thus continues to be urgent as the environmental impacts brought on by global warming become increasingly severe.[4] Hydrogen as a fossil fuel replacement has the potential to reconfigure the energy sector's use of fuel sources and usher in an era of clean energy.[5-7] However, currently, almost 95% of the estimated 55 million metric tons of hydrogen produced annually worldwide are done so using non-renewable sources (i.e., through coal or natural gas steam reforming).[7-8]

Electrolysis of water is considered to be a more environmentally sustainable approach to produce hydrogen (i.e., CO_2-emissions free when coupled with renewable energy input).[8-10] Besides, electrolysis may also play a crucial role in the storage of energy from renewable sources such as sunlight and wind.[6, 11-12] The splitting of water results from two half-reactions: the hydrogen evolution reaction (HER) and the oxygen evolution reaction (OER).[13] In an alkaline environment, the half reactions are as follows:

$$\text{Anode: } 4OH^- \rightarrow O_2 + 2H_2O + 4e^-$$

$$\text{Cathode: } 4H_2O + 4e^- \rightarrow 2H_2 + 4OH^-$$

The efficiency of water electrolysis depends on the efficiency of both HER and OER.[14] OER is the slower of the two half-reactions, as it is kinetically hindered by a multi-step-proton-coupled-electron transfer mechanism.[15-17]

Electrocatalysts increase the kinetics of OER and lower the overpotential (i.e., the applied potential required beyond the theoretical potential, E^0 = 1.23 V). Rare transition metals such as RuO_2 and IrO_2 are considered the most advanced commercially-available catalysts for OER. However, RuO_2 and IrO_2 are expensive and scarce precious metals, thus making these catalyst materials non-viable candidates for large-scale industrial manufacturing of electrolysis technology.[18-19] First-row late transition metals (e.g., Fe, Co, Ni) have recently been shown to have excellent promise as alternatives to precious metals. These first-row transition metals are less costly, widely available, stable, and insoluble in alkaline electrolytes. Besides, these metals result in catalyst materials that are highly active for OER, where the metals typically exist as oxides or hydroxides.[20-22]

Recent studies have shown that monometallic oxide and hydroxide catalysts of iron, nickel, and cobalt are not as active as their sister bimetallic or trimetallic oxide and hydroxide catalysts.[23-25] Further, bimetallic catalysts at certain ratios have been shown to complement the drawbacks of monometallic catalysts. Corrigan found that by precipitating Fe (10% at. to 50% at.) in a composite iron/nickel hydrous oxide, the Tafel slope was greatly lowered (by ~65%), indicating faster reaction kinetics for OER.[26] Tafel slope can also offer insight on the rate-limiting step, and the decrease in the Tafel slope can be associated with the surface adsorbed species formed during the initial phase of the OER remaining predominant.[27] $Fe_{0.25}Ni_{0.75}OOH$ films resulted in an increase of OER activity by 500-fold over pure Fe and Ni films,[28] while Stevens et al. were able to show an increase in activity of 150-fold for 10% Fe-containing NiO_xH_y films.[29] Finally, Louie et al. observed optimal OER activity for iron-nickel oxide thin films with 40 at.% iron composition.[30] Generally, measured overpotential also appears to be directly correlated to the FeNi atomic composition.[28, 31] The lowest OER onset potential (i.e., overpotential) was observed by Steimecke

et al. for Ni/Fe films containing 15% Fe, while Fidelsky et al. used DFT calculations to theorize that Fe-doped NiOOH are capable of lowering the overpotential by more than 40% compared to pure NiOOH.[32-33] These studies demonstrate the importance of iron incorporation into nickel-based hydroxide catalysts and suggest that the ratio of iron to nickel plays a significant role in the eventual OER activity. Several mechanisms for the improvement in OER performance have been suggested. Fidelsky et al. suggested that a band-like charge mechanism for charge transport may be present in Fe-doped NiOOH materials, which positively influences both the catalytic performance and electronic conductivity.[33] Iron doping into NiOOH has also been suggested to enhance the probability of hydrogen transfer while simultaneously requiring less activation energy.[34] DFT calculations have shown that the addition of iron dopant increases the predicted OER activity by weakening the bonds of OER intermediates.[35]

In related work, Burke et al. demonstrated that Fe incorporation in CoOOH ($Co_{1-x}Fe_xOOH$; x = 0.6-0.7) enhanced the OER activity by almost 100-fold and hypothesized that Fe is the active site for OER catalysis, while CoOOH affords chemical stability, conductivity, and electrolyte permeability for Fe active sites.[20] In the case of $Ni(OH)_2$/NiOOH, Trotochaud et al. reported that Fe incorporation in $Ni(OH)_2$/NiOOH increased the conductivity of the catalyst by more than 30-fold and indicated that Fe induces a partial-charge transfer mechanism that initiates Ni centers throughout the catalyst film, thereby increasing the OER activity of the catalyst.[31] Friebel et al. applied operando x-ray absorption spectroscopy (XAS), along with high energy resolution fluorescence detection (HERFD) and computational methods, to suggest that Fe^{3+} incorporated in $Ni_{1-x}Fe_xOOH$ increases the OER activity and that Fe sites, and not Ni sites, are the active catalytic sites in $Ni_{1-x}Fe_xOOH$.[28] As the discussion of the nature of the active site of these $Ni_{1-x}Fe_xOOH$ materials continues in the literature, thus far, it appears clear that Ni and Fe play synergistic roles

and that the active site is likely comprised of a Ni-Fe-O coordinated chemical structure. Recently, Shin et al. revealed through DFT studies that Fe^{4+} and Ni^{4+} in $Ni_{1-x}Fe_xOOH$ function as cocatalysts for OER as high spin d4 Fe^{4+} stabilizes the radical character on the O of M – O bond which subsequently facilitates O – O coupling on low spin d6 Ni^{4+}.[36] Surface metal sites (M) are largely considered to be where OER occurs, including facilitating the adsorption and reaction of a series of intermediates such as M – OH, M – O, M – OOH, M – OO.[37] However, to further complicate understanding of $Ni_{1-x}Fe_xOOH$ materials, it was recently suggested by Doyle et al.[35] that $Ni_{1-x}Fe_xOOH$ materials may have a bulk contribution to the overall observed OER activity. This computational study was based on the more ordered β-$Ni(OH)_2$, rather than the disordered alpha phase that is a closer match to the disordered $Ni_{1-x}Fe_xOOH$ materials,[31] but the results are compelling and require further inquiry.

The majority of studies thus far have focused on iron incorporated into homogeneous thin films. However, Burke et al. point to the need for high-surface-area catalysts to be developed to enable scalable catalyst and electrode development with low mass transport limitations and high mass activity performance.[37] Gorlin et al. synthesized nano-sized Ni-Fe catalysts using a microwave-assisted, surfactant-free solvothermal route and showed that Fe incorporation of around 50% resulted in the highest OER activity.[38] Further, Liu et al. managed to develop a nanostructured FeNi alloy where they incorporated S and N-doped carbon which drastically improved OER catalysis with a very low overpotential of 230mV to achieve the current density of 10 $mAcm^{-2}$.[39] Similarly, Liu et al. were also involved in the fabrication of $FeNi_3$ nanoparticles incorporated on carbon doped with multiple nonmetal elements ($FeNi_3$/M-C) that demonstrated an overpotential of 246 mV at 10 $mAcm^{-2}$.[40] Meng et al. claimed that the excellent OER performance shown by a stereo film on carbon cloth comprising $FeNi_3$ nanosheet covered FeOOH was due to

factors such as the synergistic effects of iron and nickel ratio and the availability of exposed catalytic sites for OER derived from the oxidation of the $FeNi_3$ nanosheets during the anodic oxidation.[41] Interestingly, Du et al. were able to engineer N-doped carbon coated FeNiP nanoparticles, which turned out to be a good bi-functional catalyst for alkaline water electrolysis.[42] There is now an opportunity to develop nanostructured catalysts that have similar, or better, performance metrics for OER but are amenable to scalable electrode design.

In this work, results are presented for a suite of bimetallic iron-nickel (Fe-Ni) alloy nanoparticles that are active for OER in alkaline electrolyte. To explore the role of Fe content on OER activity, Fe-Ni alloy nanoparticles were synthesized at three different molar ratios of iron to nickel. The ratios studied are mole Fe: mole Ni – 1:4, 1:1, 4:1, and will be denoted as $Fe_{20}Ni_{80}$, $Fe_{50}Ni_{50}$, and $Fe_{80}Ni_{20}$. The synthesis of these Fe-Ni bimetallic nanoparticles involved a series of precisely-timed synthesis steps in aqueous solution. Fe-Ni nanoparticles were characterized subsequently using energy dispersive x-ray spectroscopy (EDX), inductively coupled plasma mass spectrometry (ICP-MS), x-ray diffraction (XRD), and x-ray photoelectron spectroscopy (XPS). Detailed characterization was performed via synchrotron-based hard x-ray absorption spectroscopy (XAS). Transmission electron microscopy (TEM) was used for imaging morphology and diffraction analysis. From characterization results, we report new findings on the chemical and structural nature of these complex alloy nanoparticle materials. The electrochemical analysis was conducted on the Fe-Ni bimetallic catalysts using cyclic voltammetry (CV), and stability testing were performed using chronoamperometry and chronopotentiometry. The results from this work demonstrate that the ratio of iron to nickel plays a critical role in the OER activity of synthesized nanoparticles, similar to results reported for the thin films work outlined above. Activity and stability, however, must both be evaluated before a catalyst design direction is determined.

Furthermore, the results demonstrate that highly active nanocatalysts can be synthesized by a scalable synthesis process, with the potential for scale-up and industrial production of the Fe-Ni bimetallic catalysts at gram to kilogram levels.

2 EXPERIMENTAL SECTION

2.1 Materials. Chemicals were obtained as ACS grade commercial products and used without further purification unless specified. Iron(II) sulfate heptahydrate ($FeSO_4.7H_2O$), nickel(II) chloride hexahydrate ($NiCl_2.6H_2O$), amino tris (methylene phosphonic acid) (ATMP), polyvinylpyrrolidone (PVP_{40000}), sodium borohydride ($NaBH_4$), potassium hydroxide (KOH), methanol, concentrated nitric acid (HNO_3), and concentrated sulfuric acid (H_2SO_4) were purchased from commercial vendors. Ultrapure water (18.2 MΩ H_2O) was obtained from a Milli-Q Integral system installed in the laboratory. Cationic ionomer was obtained from Prof. E. Bryan Coughlin at the University of Massachusetts, Amherst and used in solution to make catalyst inks.

2.2 Nanoparticle Synthesis. Fe-Ni nanoparticles were synthesized under room temperature and atmospheric pressure conditions. All of the solutions used ultrapure deionized water as the solvent. Solutions of 29.79 g/L ATMP and 4.982 g/L of $FeSO_4.7H_2O$ were mixed at a molar ratio of 0.05: 1 in water and hand-mixed for a short time. The ATMP compound stabilizes the iron cations in solution. Separately, PVP_{40000} (molar ratio of Ni: PVP_{40000} = 1: 0.005) and $NiCl_2.6H_2O$ solutions were hand-mixed together for a short time. The amount of $NiCl_2.6H_2O$ added depends on the molar ratio of Fe and Ni desired. The first mixture of Fe/ATMP solution, along with the second mixture of Ni/PVP solution, were then transferred to a 250 mL three-neck borosilicate flask and placed on an orbital shaker. The solution inside the three-neck flask was mixed under argon gas for 15 minutes and at 100 rpm. Argon bubbling of the iron-nickel solution is performed to prevent the unwanted oxidation of the iron and nickel precursors and to control oxidation during nanoparticle formation. At approximately 13 minutes of argon bubbling, $NaBH_4$ (molar ratio of metal: BH_4^- = (1: 2.2)) aqueous solution was prepared to minimize the reaction time of $NaBH_4$ with water before adding to the iron-nickel precursor solution. The aqueous solution of

$NaBH_4$ was then added into the metal precursor solution in the three-neck flask dropwise via a syringe at a rate of approximately 30 µl/s while hand mixing the solution. Borohydride ions (BH_4^-) reduce the stabilized Fe^{2+} and Ni^{2+} ions into Fe^0 and Ni^0, respectively, forming nanoparticles during the reduction reaction. The solution in the three-neck flask was then mixed under vacuum for 15 minutes on an orbital shaker at 100 rpm. After 15 minutes of mixing, the solution in the three-neck flask was transferred to a 50 mL test tube and centrifuged for approximately 3 minutes. Supernatant from the centrifuged test tube was then decanted. The nanoparticles remaining in the test tube were mixed with 20 mL of methanol in a vortex shaker for about 30 seconds. The test tube containing the solution was again centrifuged for about 3 minutes, and the supernatant was decanted. The nanoparticles were then mixed with 20 mL of methanol and resuspended.

2.3 Characterization. Imaging was performed on an FEI Titan 80-300 transmission electron microscope (TEM) operating at 300 kV. The imaging was carried out in TEM mode. The TEM samples were prepared on TEM grids (Ted Pella Inc Formvar/Carbon 200M Cu) by diluting the nanoparticles from a concentration of 1 g/L to 0.01 g/L in methanol. 2 µL of the diluted nanoparticle solution was dropped cast on to the grid, and the methanol present in the solution was allowed to evaporate completely. Analysis of TEM images was done using Gatan™ software. Energy dispersive x-ray spectroscopy (EDX) was performed with a Nova Nanolab 200.

Inductively coupled plasma mass spectroscopy (ICP-MS) was performed using IcapQ ICP-MS (Thermo Scientific) on the Fe-Ni nanoparticles to confirm the stoichiometry in the as-synthesized materials. Each nanoparticle sample was diluted to a concentration of 50 ppb in a 2.5% nitric acid matrix. The standard curves for iron and nickel were generated using commercial ICP standards (Aristar, BDH) for each metal and diluting standard solutions to concentrations of 5, 20, 40, 60, 80, and 100 ppb. A 2.5% nitric acid matrix was used as the lab blank.

X-ray photoelectron spectroscopy (XPS) was performed on a PHI Versaprobe 5000 for each Fe-Ni nanoparticle sample to obtain a detailed chemical and elemental analysis, and the data analysis was done with the PHI MultiPack software. A monochromated Al Kα beam, along with Ar and C-60 cluster ion guns, were used. An initial scan of 0 eV to 1400 eV was carried out on the samples. This initial analysis was accompanied by detailed scans of iron (700 eV – 740 eV) and nickel (844 eV – 894 eV).

X-ray absorption spectroscopy (XAS) X-ray absorption spectroscopy (XAS) was performed on the Fe-Ni nanoparticles at a synchrotron facility in Advanced Photon Source (12-BM-B) which is a user facility branch of the Argonne National Laboratory. The samples and the standards tested for XAS were dried and suspended in a solid matrix (Kapton tape). The measurements were done around the K-edge of Fe (7112 eV) and K-edge of Ni (8333 eV). Data analysis was done using the software program Athena.

2.4 Electrochemical Measurements. All electrochemical experiments were carried out in a conventional cell at room temperature using a potentiostat (PINE WaveNow 50) in a stationary three electrodes (working electrode, counter electrode, and reference electrode) system. AfterMath software was used for data collection purpose. A gold electrode (1.6 mm Au BASi) was used as the working electrode, 3 M Ag/AgCl as the reference electrode of the cell, and a graphite rod was used as the counter electrode. The electrolyte solution for all experiments was 1M KOH. The reference electrode was placed in a salt bridge consisting of 3M NaCl solution to avoid the dissolution of the frit, as well as to prevent the formation of Ag_2O due to contact with KOH solution.

Catalyst inks were prepared for all three samples by combining the nanoparticles with a cationic ionomer at a ratio of iron to ionomer of 6:1 in methanol. The ink was then sonicated for

45 minutes in a cold-water bath to ensure a homogeneous mixture of the nanoparticle and the ionomer. 1 μL of the ink was then dropped cast on the surface of a clean Au electrode (surface area of 0.02cm^2), and the methanol was allowed to dry for 15 minutes at room temperature. The mass loading onto the electrode surface was ~50 μg/cm^2. The cleaning procedure involved the polishing of the electrode surface with alumina solutions (5 microns, 0.05 micron) on a polishing pad, followed by sonication of the electrode in DI water for 5 minutes. Next, the gold working electrode was placed in a three-electrode cell setup consisting of 0.5M H_2SO_4 as the electrolyte solution. Cyclic voltammetry was carried out in the cell for 50 cycles at 100 mV/s between -0.3V to 1.7V vs. Ag/AgCl. The working electrode was then taken out then rinsed with 18.2 MΩ DI water.

All solutions of 1 M KOH electrolyte were purified to remove trace iron impurities by following a procedure developed by Trotochaud et al.[31] In essence, to purify KOH, first, all the glassware and polypropylene centrifuge tubes that were used in the procedure were cleaned with 10 % sulfuric acid (H_2SO_4) solution. Then, 2 g of nickel nitrate hexahydrate ($Ni(NO_3)_2.6H_2O$) was dissolved with 4 mL of 18.2 MΩ DI H_2O in a tube, and 20 ml of 1 M KOH was added together and mixed to obtain nickel hydroxide ($Ni(OH)_2$) as a precipitate. The mixture was then shaken on a vortex shaker for approximately 1 minute and centrifuged. The supernatant was emptied from the tube, and three more cycles of washing $Ni(OH)_2$ precipitate with 20 mL H_2O and 2 mL of 1 M KOH were employed with each wash cycle followed by re-dispersion, centrifugation, and supernatant decantation successively. After the 3rd cycle was completed, 50 mL of 1 M KOH electrolyte to be purified was added into the tube and shaken with vortex shaker for approximately 10 minutes, and the mixture was allowed to rest for 3 hours for iron impurity removal, after which

the solution was centrifuged, and the purified 1 M KOH supernatant was decanted into an H_2SO_4-cleaned tube.

Cyclic voltammetry (CV) was conducted on the samples in a 3-electrode setup as described above. The Fe-free KOH (electrolyte solution) was bubbled with Ar gas for 30 minutes before running CVs to remove dissolved O_2. During CV experiments, a continuous flow of Ar gas was maintained in the headspace. CVs were taken between 0V and 0.8 V versus the reference electrode. 5 CV cycles were run with the clean Au electrode, and 15 CV cycles were run with the catalyst deposited on the Au working electrode. The scan rate was 20 mV/s for all CV experiments. Also, the measured potential vs. Ag/AgCl was converted to potential vs. reversible hydrogen electrode (RHE), E_{RHE}, using the following equation:

$$E_{RHE} = E_{Ag/AgCl} + 0.059*pH + E^0_{Ag/AgCl} \quad (1)$$

The measured pH of 1 M KOH was ~14. $E^0_{Ag/AgCl}$ is 0.21 V for the Ag/AgCl reference electrode in 3 M NaCl. The data was then adjusted for iR_u correction, where i is the current and R_u is the uncompensated resistance. R_u was measured using potentiostatic electrochemical impedance spectroscopy, and the values for R_u were taken at a frequency of 100 KHz. iR_u values were then subtracted from the measured potential vs. RHE. Overpotential was calculated by subtracting the theoretical potential for OER, 1.23 V, from the measured potential vs. RHE. Current measurements are reported as current density (j), where current is normalized to the geometric surface area of the Au electrode (0.02 cm^2). Chronopotentiometry and chronoamperometry were performed on the sample using the same electrochemical setup as was used to obtain CV data. Chronopotentiometry was conducted at a constant current density of 10 mA/cm^2 for 12 hours and chronoamperometry at a constant potential of 1.6 V vs. RHE for 12 hours.

3 RESULTS AND DISCUSSION

Nanoparticle morphology is shown in Figure 1. The images suggest that the nanoparticles of all three ratios tend to agglomerate together when deposited onto the TEM grid; from these results, it may be likely that the nanoparticles also similarly agglomerate on the working electrode surface. The nanoparticles appear to be roughly spherical but structurally disorganized and heterogeneous. The nanoparticles of all three ratios appear to have a mixture of both crystalline and amorphous regions. $Fe_{20}Ni_{80}$ and $Fe_{50}Ni_{50}$ may be more crystalline, compared to $Fe_{80}Ni_{20}$, as a higher content of lattice planes is observed. $Fe_{80}Ni_{20}$ had a d-spacing value of 0.211 ± 0.02 nm which was indexed to the lattice plane (111) of FeNi alloy by Li et al.[43] $Fe_{50}Ni_{50}$ had a d-spacing value of 0.196 ± 0.01 nm, and $Fe_{20}Ni_{80}$ had a d-spacing value of 0.198 ± 0.02 nm, which Ding et al. described to be approximately close to (110) planes of bcc FeNi alloy while Xia et al. indexed the d-spacing value to (111) planes of fcc γ-FeNi phase.[43-45] For all three samples, the nanoparticles have an apparent core-shell-like morphology (additional images presented in Figure S1 of the SI), but instead of one core being enclosed by a shell, multiple cores are surrounded by the same shell. From these results, we postulate that the synthesis approach causes a mixed metallic phase to form, with regions of crystallinity, where the increasing iron content causes an expansion of the lattice structure, with possible shifts in the phase present and insertion of iron into the nickel lattice likely.[31] During synthesis, the nanoparticles are exposed to water, and once synthesized, the nanoparticles are also exposed to the ambient environment. Both iron and nickel are expected to oxidize upon contact with water and oxygen, and the outer shell visible as a lighter phase contrast region in TEM imaging is likely an oxidized layer that forms on the bimetallic core nanoparticles. Line scans and point measurements of nanoparticles (Figure S1) identify both iron and nickel in the shell and support this conclusion.

All three ratios of iron-nickel nanoparticles appear to have a relatively similar size, thus indicating that the ratio between the two metals in the bimetallic composition does not control the overall size of the nanoparticles during the synthesis process. Often, the ratio between the metal precursors and the stabilizers used (e.g., ATMP, PVP) plays a bigger role in controlling the particle size of nanoparticles synthesized through solution-phase chemistry techniques, such as our aqueous-based chemical reduction technique.[46]

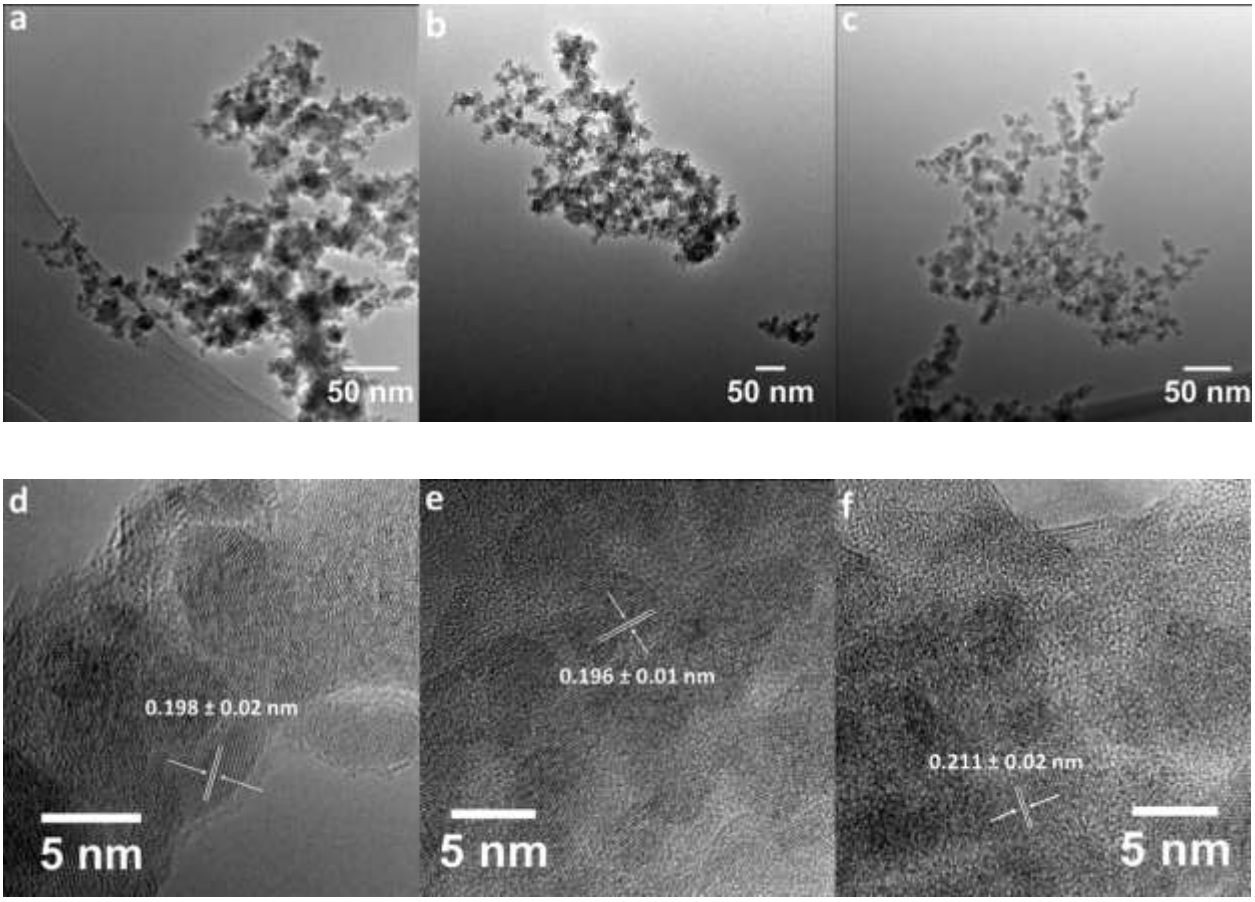

Figure 1. TEM and HRTEM images of synthesized alloy nanoparticles: a) & d) $Fe_{20}Ni_{80}$, b) & e) $Fe_{50}Ni_{50}$, and c) & f) $Fe_{80}Ni_{20}$.

Due to the complexity of the nanoparticle morphology, a suite of characterization tools was used to investigate elemental composition (summarized in Table 1). The purpose of the suite of measurements was to determine possible differences between the observed core and shell structures, as well as to compare methods that provide bulk versus surface-sensitive measurements. SEM EDX was used to obtain elemental information, where the spectra represent an overall average measurement from a large population of nanoparticles. TEM EDX point measurements were made on individual nanoparticles for both the observed darker core region and the observed lighter phase contrast shell encapsulating the cores. While EDX, in general, is a highly useful characterization tool, all EDX measurements are at most semi-quantitative and thus should be used to compare within a sample set and should always be compared to more quantitative measurements. Both ICP-MS and XPS characterization were used to compare to EDX measurements. ICP-MS is a precise and quantitative measurement tool, but is a bulk measurement of the metals in the sample and cannot measure oxygen content. Finally, XPS is surface sensitive and measures a large particle population, but is considered to be a more precise quantification of composition within a comparative sample set, as compared to EDX. X-ray diffraction (XRD was also used to characterize the samples, and the result is presented in the SI. Thus, the combination of these techniques can provide an overall understanding of the nanoparticle bulk and surface composition, the relative amount of oxygen in the sample (which can include contributions from ligand stabilizers), the atomic ratio of iron to nickel, and any discrepancies between individual versus populations of particles.

The elemental analysis from SEM EDX of the three ratios of iron-nickel nanoparticles is summarized in Table 1, for the relative amounts of iron and nickel in each sample. In the data shown in Table 1, iron and nickel atomic % are reported out of 100%; other minor components

(e.g., salt contaminants from synthesis such as sodium and chloride) and oxygen content are not reported. As a semi-quantitative measurement, EDX is primarily used herein to compare relative ratios of Fe: Ni between samples synthesized in this work. Our EDX measurements during SEM imaging verify that the ratios measured in the synthesized nanoparticle samples match the theoretical target ratios of precursors used in the synthesis procedure. The Fe: Ni ratios reported in Table 1 are below the expected EDX margin of error of 10%, compared to the theoretical target molar ratios (i.e., 5:1, 1:1, and 1:5) for all three nanoparticle samples. EDX measurements thus corroborate the initial calculations used for the synthesis of different molar ratios of nanoparticles and demonstrate that the samples tested contained the target Fe concentrations. A more detailed table of SEM EDX for both atomic and weight % is reported in the Supplemental Information (SI).

TEM EDX analysis was performed as a series of point measurements. TEM dark field images of the point measurement locations are reported in the SI, and the elemental composition data are summarized in Table 1. Several interesting observations can be made from these data, as well as when these data are compared to SEM EDX data. First, there are measurable differences in the oxygen content of the core versus the shell, where the shell of all three samples has significantly higher oxygen atomic % than the core. These results are consistent with the observable phase contrast between the core and shell for all three samples in Figure 1 and Figure S1, where a darker phase contrast typically indicates a larger metal content. Second, the $Fe_{50}Ni_{50}$ composition does not result in measurable differences in iron to nickel ratio in the core versus the shell, whereas $Fe_{20}Ni_{80}$ has a slightly higher content of nickel in the shell than the core. Interestingly, the iron content in the shell compared to the core for $Fe_{80}Ni_{20}$ was much larger, and both measured ratios of Fe: Ni were greater than the bulk ratios obtained from SEM EDX and ICP, as well as greater than the surface ratio of Fe: Ni as measured by XPS. This discrepancy may

indicate particle-to-particle variability. Finally, the measured iron to nickel ratios are, overall, generally consistent with the target theoretical ratios intended during synthesis. As mentioned above, the aqueous synthesis method does allow some exposure to oxygen as well as direct exposure to water molecules during synthesis, and the synthesized nanoparticles are also exposed to the ambient atmosphere after synthesis. Our characterization data presented in Table 1 further support the initial conclusion based on TEM imaging that exposure to oxygen and water likely enables the formation of a more oxygen-rich shell, with associated oxide or hydroxide formation as well as metal migration and restructuring. We do not currently understand when the shell structure forms or exactly how the morphology changes during or after synthesis. However, the result is a complex and heterogeneous morphology with direct implications for OER performance and catalyst stability.

Analysis of the data collected by ICP-MS is used to quantitatively account for the metal compositions (iron and nickel) of the samples. The raw data provided by the instrument gave counts per second for iron and nickel, which was then converted into concentration at parts per billion (ppb) (reported in SI). The concentrations in μM for iron and nickel were obtained by dividing concentrations in ppb by the molecular weight of their respective isotopes (57 Fe for iron and 60 Ni for nickel). The molar ratio of Fe:Ni was obtained by dividing the concentration of iron in μM by that of nickel in μM. The molar ratios of $Fe_{20}Ni_{80}$, $Fe_{50}Ni_{50}$, and $Fe_{80}Ni_{20}$ obtained from ICP-MS were below a margin of error of 10% in comparison to the targeted theoretical molar ratios during synthesis for all three nanoparticle samples. Also, the ratios measured by ICP-MS are the same as those measured by SEM EDX. Along with EDX results, ICP-MS results thus provide an additional verification that the composition of iron and nickel in all three nanoparticle samples was reflective of the desired molar ratios from a bulk particle perspective.

Table 1. Comparison of elemental composition analysis results from bulk and surface-sensitive techniques. All ratios are given as Fe:Ni.

Sample	SEM EDX Atomic %			TEM EDX Atomic %			TEM EDX Atomic %			ICP Atomic %		XPS Atomic %		
	Multiple Particle Average			Individual Particle Core			Individual Particle Shell			Bulk Sample Average		Surface Sample Average		
	Fe	Ni	O	Fe	Ni	O	Fe	Ni	O	Fe	Ni	Fe	Ni	O
$Fe_{20}Ni_{80}$	9	42	49	9	38	53	4	21	75	18	82	16	44	40
$Fe_{50}Ni_{50}$	25	25	50	18	19	63	9	11	80	50	50	25	29	46
$Fe_{80}Ni_{20}$	45	9	46	38	5	57	11	1	88	83	17	40	9	51

Surface elemental composition of the nanoparticle samples was determined by XPS, which is a highly surface sensitive tool that analyzes to a depth of <10 nm of a surface.[47] For the nanoparticle morphology and size scale shown in Figure 1, XPS measurements likely probed both the surface oxide shell and the core. For a nanoparticle sample, XPS measures a population of nanoparticles in a nanoparticle film, and one might expect some variability in nanoparticle packing with resulting variability in the microscopic topology of the film. This variability can result in variability in the actual depth of the XPS measurement into the sample, and thus, our results may represent an average of surface and subsurface composition. Survey spectra lines (reported in SI) were analyzed to calculate relative elemental concentration for Fe, Ni, O, C, and N. All trace

elements present in the samples were discarded from the summation presented in Table 1, but are reported in the SI. All three nanoparticle samples contained a substantial amount of oxygen, as was also suggested by the TEM EDX results. However, the oxygen content estimated by XPS measurements is less relative to iron and nickel, as compared to TEM EDX point measurements of the shell regions and is rather more similar to the oxygen content measured for the cores of the nanoparticles. This result could suggest there may be a potential overestimate in relative oxygen content by the TEM EDX measurements and also suggests there is reduced metal content in the subsurface of the nanoparticles, which is not surprising given that the synthesis technique relies on the chemical reduction of both metal cation precursors by borohydride to form particles. However, we propose that the TEM EDX measurements are not an overestimate and that the XPS measurements are, in this case, not solely measuring the surface of the nanoparticles. Given that XPS will probe approximately 3-5 nm into the surface of the nanoparticles, and the shell morphologies observed in Figure 1 and Figure S1 is on the order of ~2 nm, it is likely that the XPS data are reflective of a combined surface and subsurface chemical composition, while the TEM EDX data of the shell is more reflective of just the shell composition. If we make this assumption, we can evaluate the metal to oxygen ratio and begin to develop a picture of the surface chemistry. For the $Fe_{20}Ni_{80}$ composition, the ratio of metal to oxygen is 25 to 75, while for the $Fe_{50}Ni_{50}$ composition, the ratio of metal to oxygen is 20 to 80 and for $Fe_{80}Ni_{20}$, the ratio is 12 to 88. The two compositions with lower Fe content thus have a metal (M) to oxygen (O) ratio, M:O, of ~1:3 - ~1:4. These ratios are higher than what would be expected for a nominal oxide or hydroxide based on an iron-incorporated nickel host phase, but might suggest that the phase is more likely to be similar to an iron-incorporated nickel hydroxide ($Fe_xNi_{100-x}(OH)_2$) rather than a nickel oxide (NiO) or an iron oxide (e.g., Fe_2O_3). Since we believe that the shell measurement for the $Fe_{80}Ni_{20}$

composition is slightly off based on our other measurements, we assume at this point in the analysis that the higher iron content composition has a similar initial surface phase as the other as-synthesized nanoparticle compositions. Overall, these results likely point to some extent of overestimation of oxygen content by TEM EDX, where the analysis of low atomic weight elements such as oxygen is less reliable than the analysis of metal species. The combination of our TEM EDX and XPS results can be used as complementary techniques to probe the surface, subsurface, and bulk chemical character of as-synthesized nanoparticles. The results also illustrate the importance of using and understanding multiple characterization tools to characterize morphologically-complex nanomaterials.

The oxygen present in the surface of nanoparticle samples can thus likely be attributed to metal hydroxides, with a minor contribution from the oxygen atoms attached to the organic ligands (ATMP and PVP) that were used as stabilizers during nanoparticle synthesis.[48] It is not expected that there would be a significant contribution from ambient organic contamination to the oxygen signal because the samples were cleaned and stored in methanol until prepped for XPS measurements. The amount of carbon is approximately equal in the three nanoparticle samples, while nitrogen accounts for a smaller percentage. Both carbon and nitrogen can be traced back to the use of organic compounds (ATMP and PVP) that could not be completely rinsed off after synthesis. The XPS-measured iron and nickel content in $Fe_{80}Ni_{20}$ and $Fe_{50}Ni_{50}$ match relatively closely with the SEM EDX results (Table 1) for the same sample while the amount of nickel in $Fe_{20}Ni_{80}$ is 40% lower in comparison to the SEM EDX results.

High-resolution XPS was performed on both iron and nickel regions to further understand the oxidation state of the metal species in the nanoparticles (Figure 2). The Fe 2p region for the three nanoparticles show a shift in Fe $2p_{3/2}$ peaks, but the Fe $2p_{1/2}$ peak positions are similar for all three

samples. The Fe $2p_{3/2}$ peak was observed at 710.8 eV for $Fe_{80}Ni_{20}$ (Fig. 2a), which can be attributed to both iron oxide and hydroxide species. For $Fe_{50}Ni_{50}$, the $Fe2p_{3/2}$ peak (Fig. 2c) was at 711.4 eV, which suggests iron is likely present as iron hydroxide in either the alpha or gamma phase. Similarly, $Fe_{20}Ni_{80}$ has a $Fe2p_{3/2}$ peak at 711.8 eV (Fig. 2e), which also points toward the presence of an alpha or gamma hydroxide species. The $2p_{1/2}$ peak positions for $Fe_{80}Ni_{20}$, $Fe_{50}Ni_{50}$, and $Fe_{20}Ni_{80}$ were located at 724.2 eV, 723.9 eV, and 724.0 eV, respectively, which collectively can be attributed to both iron oxide and hydroxide species.[49-51] For $Fe_{80}Ni_{20}$, there appears to be a small peak around 707 eV which indicates the presence of some iron metal species at an oxidation state of 0. Neither $Fe_{50}Ni_{50}$ or $Fe_{20}Ni_{80}$ composition had a distinct iron metal peak, but both spectra have a broadening of the Fe $2p_{3/2}$ peak between 708 eV and 703 eV, suggesting that there is a metallic contribution to the chemical environment of the iron atoms. The lack of a distinct metal peak may result from the inherent variability of the nanoparticle film and the probing depth of the XPS technique, which includes both the shell and a portion of the bulk underneath the visible shell. The nanoparticles are also exposed to the atmospheric conditions which could result in oxidized surfaces, and since XPS is a surface sensitive technique, the spectra could not account for the metallic region that might be present underneath the oxidized surfaces. Since the lack of distinct metal peak occurred in the two nanoparticles with higher nickel content, $Fe_{50}Ni_{50}$ and $Fe_{20}Ni_{80}$, the iron metal signal could have been suppressed by the greater amount of nickel that is present in the surface of the two nanoparticle films.

In the Ni 2p region, all three nanoparticles had bulk metal content, which supports the compositional analysis discussed above. Unlike the iron spectra, the nickel spectra all display a sharp, distinct peak for the metallic nickel. The peaks at 852.2 eV, 852.3 eV, and 852.0 eV for $Fe_{80}Ni_{20}$, $Fe_{50}Ni_{50}$, and $Fe_{20}Ni_{80,}$ respectively, can be classified as nickel metal peaks. The Ni $2p_{3/2}$

peak at 855.6 eV was observed for $Fe_{80}Ni_{20}$, but the Ni $2p_{1/2}$ peak was not distinguishable from the noise. Ni $2p_{3/2}$ peaks for $Fe_{50}Ni_{50}$ and $Fe_{20}Ni_{80}$ were observed at 855.6 eV and 855.4 eV, respectively, and the nearly identical peak locations suggest that the nickel chemical environment is similar in all three samples. The Ni $2p_{3/2}$ peaks for all three nanoparticles suggest the presence of nickel hydroxide. The Ni $2p_{1/2}$ peak for $Fe_{50}Ni_{50}$ was located at 873.0 eV and similarly for $Fe_{20}Ni_{80}$ at 873.2 eV, which suggests the presence of nickel oxide.[25, 48, 52-53] The peak positions for both iron and nickel spectra for all three nanoparticles are within a similar range of one another which suggests that the speciation and oxidation state are similar between the three samples. With the XPS results for the three nanoparticles, a case can be made for iron to be primarily in a +3 oxidation state, with a minor contribution from Fe^0, whereas nickel is primarily in a +2 oxidation state, with some of the nickel content in the 0 oxidation state.

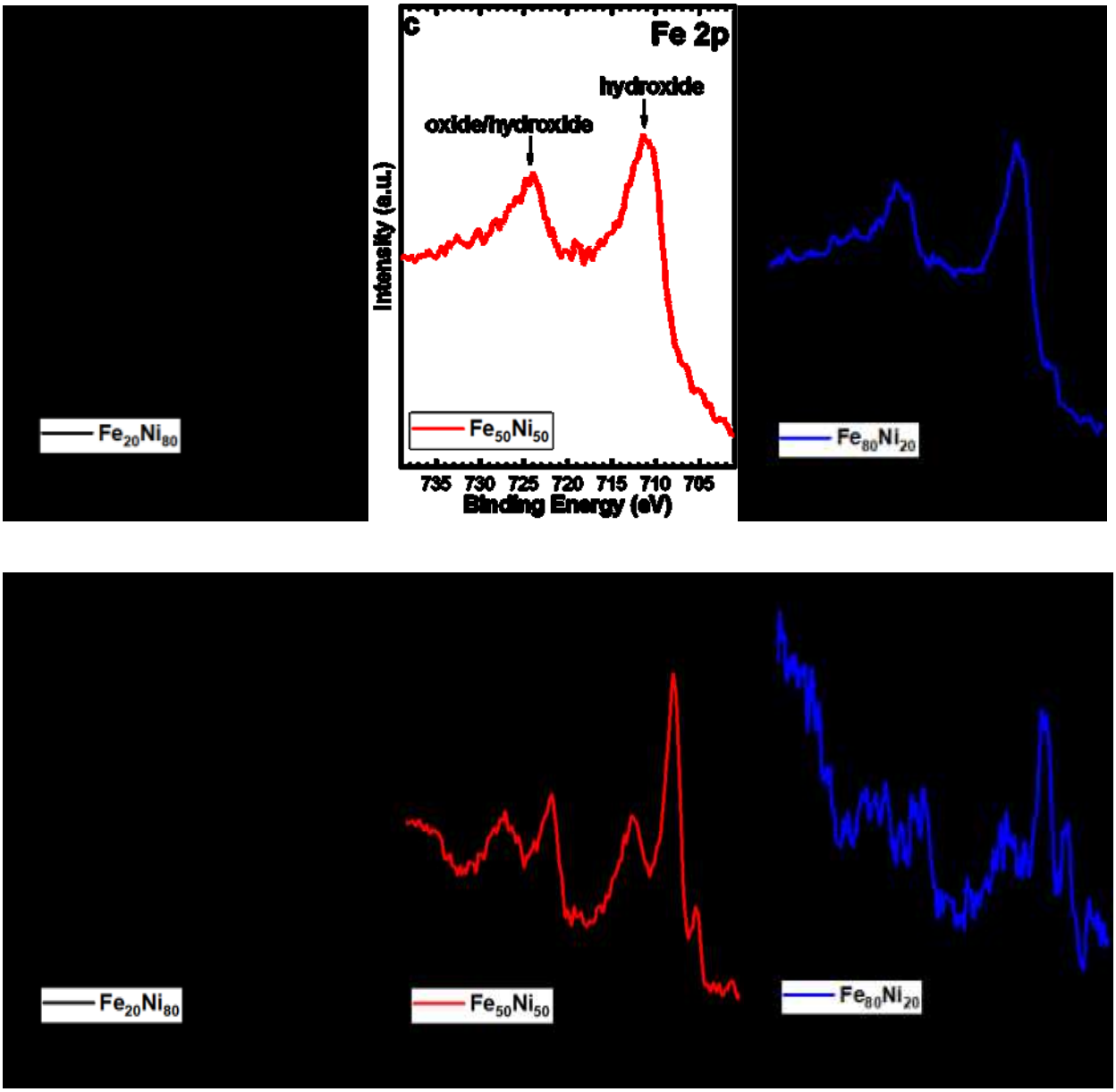

Figure 2. XPS spectra of (a) Fe 2p for $Fe_{20}Ni_{80}$, (b) Ni 2p $Fe_{20}Ni_{80}$, (c) Fe 2p for $Fe_{50}Ni_{50}$, (d) Ni 2p for $Fe_{50}Ni_{50}$, (e) Fe 2p for $Fe_{80}Ni_{20}$, (f) Ni 2p for $Fe_{80}Ni_{20}$.

To further understand the chemistry of the nanoparticles, x-ray absorption spectroscopy (XAS) was performed. Unlike XPS, which is a surface characterization tool, XAS is a bulk characterization technique. XAS data can be classified into three different regions: pre-edge region, x-ray near edge spectroscopy (XANES), and extended x-ray absorption fine structure

(EXAFS). XANES data are reported in Figure 3. XANES data for the iron K edge region show that all three samples qualitatively appear similar with only minor differences in the spectra. The Fe K edge spectra for $Fe_{80}Ni_{20}$ and $Fe_{50}Ni_{50}$ virtually overlap on top of each other. The Fe K edge of $Fe_{20}Ni_{80}$ has higher intensity at the main absorption peak and slightly lower intensity at the pre-edge, compared to the $Fe_{80}Ni_{20}$ and $Fe_{50}Ni_{50}$. Out of the three standards shown, only the pre-edge feature of metallic iron is slightly similar to that of the three nanoparticle samples, while the other two standards have much more distinct pre-edge features (additional standards are reported in the SI). Generally, the weak pre-edge feature, which corresponds to 1s→3d electronic transitions, can be seen in both the iron and nickel regions for the three nanoparticle samples and is potentially indicative of octahedral coordination,[54-57] but a more in-depth analysis suggests, particularly for iron, that the XAS measurement is a combination of multiple iron chemical environments and, potentially, multiple coordination environments.

For iron specifically, the pre-edge shape and position suggest contributions from metallic iron and Fe^{3+}, where the position matches the pre-edge peak position of the $Fe(OH)_3$ reference, but the shape of the pre-edge is more reflective of a lower-intensity iron metal pre-edge. The Fe metal reference material was an iron foil, with bulk bcc crystal structure and iron atoms in a tetrahedral geometry. The ferric hydroxide reference, also known as goethite, had a closed packed hexagonal structure, where iron atoms occupy octahedral positions within the hydroxide structure. The nickel ferrite ($NiFe_2O_4$) reference is known to have an inverse spinel face-centered cubic (fcc) crystal structure, where the divalent nickel occupies only octahedral sites, while trivalent iron equally occupies both octahedral and tetrahedral interstitial sites within the crystal structure.[58] In addition to the oxidation state, the pre-edge feature can also provide information about the metal coordination geometry[59] of a material. Comparison to these reference spectra pre-edge peak shape

and positions suggests that iron atoms that are in the +3 oxidation state may be chemically situated in an octahedral coordination environment, while a population of the iron atoms may be in a zero valent metallic state. However, the coordination environment of the zero valent iron atoms is unlikely to be a simple bcc coordination like that of bulk iron metal. Given the lattice spacing results from TEM imaging and the possibility that internal iron and nickel atoms are in a metallic alloyed phase, we consider the impact of iron composition on the crystal structure of iron-nickel alloys. Mckeehan reported in 1923[60] on the effect of composition on FeNi alloy crystal structure, where for iron atomic compositions of 70% or less, the alloy takes an fcc crystal structure with octahedral coordination, while for iron compositions of greater than 75%, the alloy phase takes on an iron-like bcc crystal structure with tetrahedral coordination. Based on this work, the iron atoms in a metallic oxidation state are likely to be coordinated more similarly to octahedral coordination chemistry for the $Fe_{20}Ni_{80}$ and $Fe_{50}Ni_{50}$ compositions but may be more likely to be closer to tetrahedral geometry for the $Fe_{80}Ni_{20}$ composition. The challenge with our nanoparticles is that XAS analysis is a bulk characterization technique and averages morphologically and chemically distinct regions of our nanoparticles into one single spectrum. While other studies[28, 38, 59] can model XAS data based on a singular phase, we know that our nanoparticles have a multi-region morphology with distinct phases likely. Thus our analysis remains qualitative, but characterization through XAS does provide additional detail about potential phases and metal coordination that is not possible with the other techniques presented herein.

The main Fe K edge absorption peak of $Fe_{20}Ni_{80}$ aligns well with that of $Fe(OH)_3$ whereas the primary Fe K absorption peak for $NiFe_2O_4$ is quite similar in shape to that of $Fe_{50}Ni_{50}$ and $Fe_{80}Ni_{20}$. This difference is perhaps the most significant when the three FeNi nanoparticle samples are compared. Both reference materials have iron in the 3+ oxidation state; none of the three

experimental sample Fe K edges are at all similar to the Fe K edge of the iron foil reference. From the XANES region of Fe K edge, a strong case can be made for the majority of the iron atoms in our nanoparticles to be primarily in +3 oxidation with low contributions from metallic iron, with perhaps a small contribution of iron atoms in the 0 oxidation state.

Similarly, the XANES data for the nickel region of the three samples have almost identical spectra with a slight exception of $Fe_{20}Ni_{80}$ having a moderately higher normalized intensity. The Ni K edge spectra of $Fe_{50}Ni_{50}$ and $Fe_{80}Ni_{20}$ are effectively the same. In comparison to the pre-edge of the three standards, only the metallic nickel feature had resemblance with the three nanoparticles. The pre-edge features of the other two standards, β-$Ni(OH)_2$ and $NiFe_2O_4$, are very distinct in comparison to that of the three nanoparticles and the Ni metal foil reference. The samples show metal-like pre-edge feature, but interestingly very high white-line intensity which expected in oxidized Ni. The main absorption peaks for $NiFe_2O_4$ and β-$Ni(OH)_2$ have absorption energies in the same range as the three nanoparticle samples but with higher normalized intensity.

Nickel foil was used as a reference for the nickel metal and had an fcc crystal structure. β-$Ni(OH)_2$ has a hexagonally closed packed-structure of Ni^{2+} and OH^- and is the more stable polymorph of $Ni(OH)_2$.[61] β-$Ni(OH)_2$ is found naturally as the mineral theophrastite and is isostructural with brucite ($Mg(OH)_2$).[62] In β-$Ni(OH)_2$, each Ni atom is surrounded by six O atoms to form an octahedral structure. The symmetry of the metal-ligand cluster is the determining factor for the existence and intensity of the pre-edge features.[63] McBreen et al. further suggested that in a pure octahedral configuration, no pre-edge feature should be present at all owing to the center of inversion of the octahedron. Thus, weak pre-edge features only arise with the distortion of the octahedral environment, which leads to the removal of the center of inversion of the symmetry.[63] The presence of broad pre-edge peaks for the nanoparticles could be indicative of Ni distorted

octahedral coordination.[64] Kim et al. also suggested that small magnitude of pre-edge features can be emblematic of distorted octahedral coordination.[57] Similar to the alpha phase of $Ni(OH)_2$, β-$Ni(OH)_2$ can also be classified as an insulator and bulk $NiFe_2O_4$ also behaves as an insulator.[62, 65-66] Unlike in metals, where the screening of core-hole electron is usually complete, the core-hole electron is only partially screened in insulators. Due to the photo-electron core hole interactions in these nickel oxides (insulators), pre-edge features can be influenced by molecular orbitals of the cluster formed by absorbing and backscattering atoms. Therefore, Mansour et al. cautioned against the direct comparison of pre-edge regions in nickel metal and nickel oxides.[64] Thus, for all three nanoparticle samples, which lacked a distinct pre-edge feature and had only weak and broad spectra, we conclude that the pre-edge shape is the result of the nanoparticles having nickel in distorted octahedral configuration. The pre-edge shape and position strongly align with metallic nickel, but judging by the main absorption peak position, both β-$Ni(OH)_2$ and $NiFe_2O_4$, which have an oxidation state of +2 for Ni, closely match with the three nanoparticle samples. However, the intensities of the main absorption peaks of the three nanoparticle samples are lower than both β-$Ni(OH)_2$ and $NiFe_2O_4$ references. Numerous variables, which include charge density, ligand symmetry, and spin density, can affect the XANES spectra, but the absorption edge position can be a reliable indicator of the oxidation state in nickel.[67-68] Therefore, taking into account the pre-edge and XANES spectra points to a mixed oxidation state of +2 and 0 for nickel, where nickel atoms in the +2 oxidation are likely the majority species at both the bulk and also the surface of the nanoparticles, as seen through XPS results, while some amount of metallic nickel is prominent in the bulk. Given the known difference in the standard reduction potentials for both Fe^{2+} (E^o = -0.44 V) and Ni^{2+} (E^o = -0.23 V), the latter is more likely, as the reduced iron species will preferentially donate electrons to the nickel cations present, causing a reduction to the zero

oxidation state. This thermodynamically favorable reaction thus results in the oxidation of the iron metal to a ferrous iron cation. The iron and nickel spectra of three nanoparticle samples having closely related features could be explained by the fact that the synthesis process used was identical regarding salt precursors, ligand stabilizers, reducing agents, and general procedure. XANES data thus give a great insight into the atomic level chemistry of the nanoparticles and thus gives a basis for further investigation of bimetallic iron-nickel nanoparticles for enhanced OER performance.

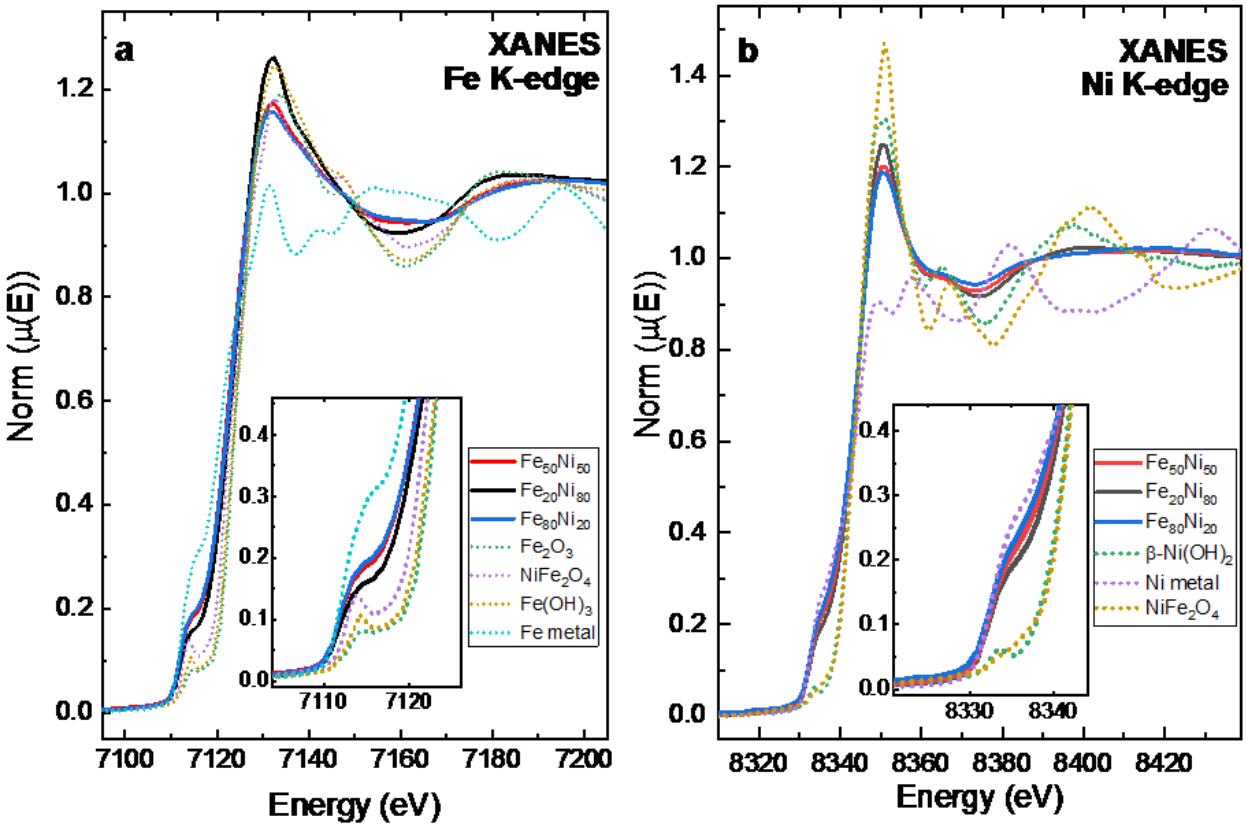

Figure 3. XANES region of the (a) Fe K-edge and the (b) Ni K-edge.

The results of the electrochemical analysis done on the iron-nickel nanoparticles using CV are shown in Figure 4(a). $Fe_{20}Ni_{80}$ had the lowest onset potential, followed by $Fe_{50}Ni_{50}$ and $Fe_{80}Ni_{20}$. The same trend held for the potential required to achieve a benchmark current density (j)

of 10 mA/cm^2. The overpotentials for $Fe_{20}Ni_{80}$, $Fe_{50}Ni_{50}$, and $Fe_{80}Ni_{20}$ were 313 mV, 327 mV, and 364 mV respectively at 10 mA/cm^2 (Figure 4(b)). Another benchmark used to test the catalysts in OER is to measure the current density at an overpotential (η) of 300 mV. $Fe_{20}Ni_{80}$ yet again outperformed $Fe_{50}Ni_{50}$ and $Fe_{80}Ni_{20}$. The current density of $Fe_{20}Ni_{80}$ had a current density of 4.92 mA/cm^2, which was followed by $Fe_{50}Ni_{50}$ with 3.43 mA/cm^2 and $Fe_{80}Ni_{20}$ with 0.54 mA/cm^2. However, at an overpotential (η) of 450 mV, $Fe_{50}Ni_{50}$ outperformed the other two catalysts as it reached current density (j) of 207 mA/cm^2 while $Fe_{20}Ni_{80}$ and $Fe_{80}Ni_{20}$ managed current densities (j) of only 150 mA/cm^2 and 131 mA/cm^2, respectively. Based on those three standards (j = 10mA/cm^2, η = 300 mV, and η = 450 mV), it can be inferred that the iron-nickel nanoparticle with lowest iron proportion of iron is the most active at lower overpotential and the nanoparticle having iron quantity of 50% is only slightly less active at lower overpotential but had the highest current density at greater overpotentials. This switch in the best-performing composition is particularly important when one considers that an electrolysis cell would be operating at elevated current densities beyond 10 mA/cm^2.[69] $Fe_{80}Ni_{20}$, with the highest amount of iron, performed significantly worse than the other two nanoparticles. The result obtained in this study closely mirrors the ones in the literature for nickel-based thin films. Corrigan et al. observed that a sweet spot existed for the iron addition in nickel thin films which occurred between 10% and 50%, while Louie et al., Friebel et al., and Trotochaud et al. independently came to the same conclusion.[26, 28, 30-31] We find it fascinating that the relationship between the ratio of iron to nickel and the OER catalytic performance that exists for the FeNi hydroxide thin films also holds in this study for nanoparticles, but it is also compelling that our results suggest the recent literature benchmarks for OER (i.e., measurement of overpotential at 10 mA/cm^2 and measurement of current at 300 mV of overpotential) are perhaps not appropriate for selecting optimal OER catalysts nor for necessarily

selecting directions for catalyst development and design. Instead, we recommend considering a second set of metrics at potentials relevant to commercial electrolysis, such as those tested in Speck et al.[69] At a current density of 100 mA/cm^2, our nanoparticle catalysts resulted in overpotentials of 415 mV, 391 mV, and 436 mV for $Fe_{20}Ni_{80}$, $Fe_{50}Ni_{50}$, and $Fe_{80}Ni_{20}$, respectively. Interestingly, the gap between $Fe_{20}Ni_{80}$ and $Fe_{80}Ni_{20}$ is even lower when the catalysts reached a current density of 150 mA/cm^2. At a current density of 150 mA/cm^2, our nanoparticle catalysts resulted in overpotentials of 450 mV, 415 mV, and 457 mV for $Fe_{20}Ni_{80}$, $Fe_{50}Ni_{50}$, and $Fe_{80}Ni_{20}$, respectively. Prior work by our group has evaluated the electrochemical surface area (ECSA).[70] Turnover frequency (TOF) was calculated for each sample and the result is shown in Table S5. A CV graph of IrO2, a reference catalyst for OER, is shown in figure S8.

Our performance data generally suggest that the nanoparticles synthesized herein may be in some respects a close replica of advanced iron-nickel based thin films, which is a similar conclusion to our prior work.[48] An interesting feature of nickel-based catalysts for OER is the presence of the nickel redox peak before the OER onset potential. $Fe_{20}Ni_{80}$ had a large nickel redox peak while $Fe_{50}Ni_{50}$ had a notably smaller peak and $Fe_{80}Ni_{20}$ had virtually nonexistent nickel redox peak. The size of the peak is proportional to the nickel content in the nanoparticles. In $Fe_{20}Ni_{80}$, which had the earliest OER onset potential among the three nanoparticles, the nickel redox peak occurred at the lowest potential. The second most active catalyst $Fe_{50}Ni_{50}$ had nickel redox peak at a slightly higher potential than $Fe_{20}Ni_{80}$. The trend observed in our work suggests that an increase in nickel content (decrease in iron content) shifts the nickel redox peak to occur at a lower potential. The difference in oxidation peaks between $Fe_{20}Ni_{80}$ and $Fe_{50}Ni_{50}$ was around 40 mV. Similarly, Louie et al. noted that the incorporation of iron into nickel hydroxide films shifted the nickel redox peak towards higher potentials, and the amount of iron was linearly proportional to

the shift in potential and inversely proportional to the redox area, i.e., increase in the iron content in the film directly corresponded to the higher potentials at which the redox peaks occurred.[30] Louie et al. implied that increasing iron content led to the shift in nickel redox peak towards higher potential, which in turn resulted in the suppression of electrochemical oxidation of $Ni(OH)_2$ to NiOOH by iron.[30] The result obtained by Louie et al. confirmed the trend observed in our results. In Corrigan's work, between 0% Fe containing nickel oxide film and 10% Fe containing nickel oxide film, the nickel redox couple for iron-containing film increased by almost 50 mV and the redox couple area was visibly decreased.[26] Lu et al. observed the same trend for NiFe layered double hydroxide (LDH) where $Ni(OH)_2$/NiOOH redox couple shifted to higher potential and the redox area decreased compared to just a $Ni(OH)_2$ film which they attributed to inhibition of Ni^{2+} to Ni^{3+} conversion by highly charged Fe^{3+} ions which occupied the neighboring spaces.[71] Hu et al. claimed that the OER activity for Fe-Ni materials could be reliably predicted by nickel redox peak that occurs before OER and that the nickel redox peak is strongly dependent on the composition of Fe-Ni which also controls the overall activities of OER. Similar to our work, Hu et al. observed that the nickel redox peak shifted towards more positive potential with increasing iron content.[72] Li et al. also observed the nickel redox peak shift towards more positive potential for Ni/$Fe(OH)_2$ film in comparison to $Ni(OH)_2$ film and asserted that the oxidation potential in a mixed Ni/$Fe(OH)_2$ is actually determined by the potential of Fe(III)/Fe(IV) conversion as $Fe(OH)_3$ is a poor conductor until it is converted into higher oxidation state.[73] Similar to our work where $Fe_{80}Ni_{20}$, which contained a high amount of iron did not show any redox peak, Bates et al. also observed a muted redox peak for their Fe/Raney Ni and suggested that the iron-rich surfaces do not increase OER activity as much as other iron-nickel based catalysts.[23] To address the phenomenon of iron affecting nickel redox properties, Gorlin et al. theorized that negatively charged oxygen ligands

are formed in iron centers which suggests a transformation from a two proton-two electron process to a two proton-one electron transfer.[74]

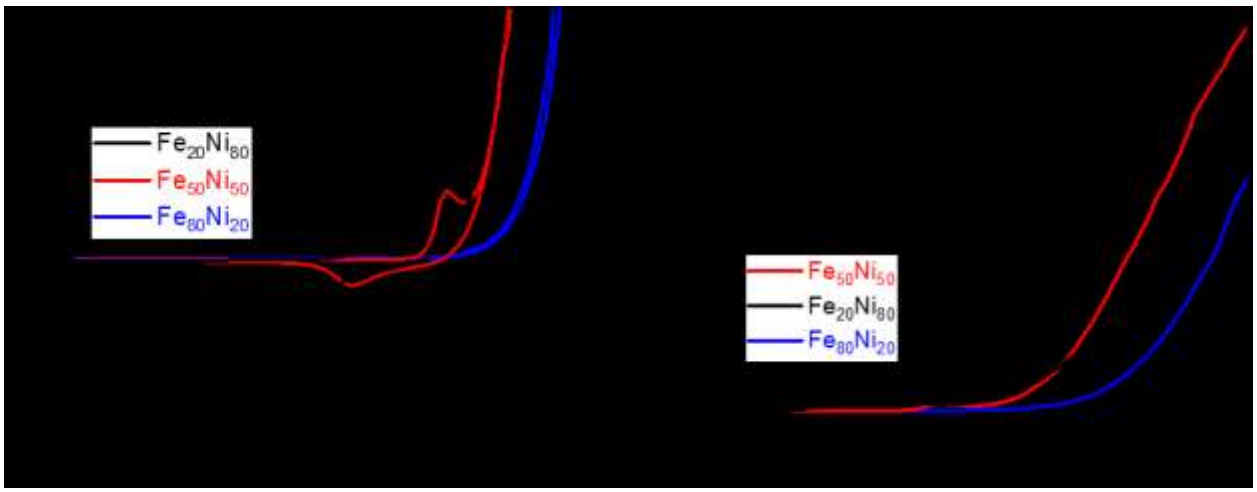

Figure 4. (a) & (b) CV scans of Fe-Ni NPS in 1M KOH electrolyte solution after 20 cycles

Chronoamperometry (CA) and chronopotentiometry (CP) data are presented in Figure 5, with a summary of performance metrics in Table 2. CA was conducted at a constant potential of 1.6 V vs. RHE, and CP was performed at a constant current density of 10 mA/cm^2. Observing the CA data, $Fe_{80}Ni_{20}$ is the most stable catalyst throughout the 12 hours with a degradation rate of -0.003 mA/hr. The overall degradation rate of $Fe_{50}Ni_{50}$ was -0.025 mA/hr, while $Fe_{20}Ni_{80}$ was the most unstable catalyst out of the three tested, with a degradation rate of -0.026 mA/hr. Interestingly, the CA results are inverse in trend compared to the OER activity results obtained through the CV. Both $Fe_{20}Ni_{80}$ and $Fe_{50}Ni_{50}$ compositions, which had the lowest onset OER potentials, were much more unstable than $Fe_{80}Ni_{20}$, which had the largest onset OER potential among the three. CP data in Figure 5 also indicates the same stability trend of the nanoparticle

catalysts. $Fe_{80}Ni_{20}$ was the most stable with a degradation rate of 0.017 mV/hr, followed by $Fe_{50}Ni_{50}$ with a 0.951 mV/hr degradation rate, and $Fe_{20}Ni_{80}$ with a 1.288 mV/hr degradation rate. Tafel slopes for the three catalysts are plotted in Figure 5c. $Fe_{50}Ni_{50}$ had the lowest Tafel slope of 44.2 mV dec^{-1} followed by $Fe_{80}Ni_{20}$ with a Tafel slope of 48.6 mV dec^{-1}, and $Fe_{20}Ni_{80}$ had the highest Tafel slope of 62.5 mV dec^{-1}. Tafel slopes for all three nanoparticle catalysts being less than 120 mV dec^{-1} rules out the prevalence of surface species that were formed a step earlier than the rate determining step.[27] A Tafel slope value of 40 mV dec^{-1} demonstrates that there is a pre-equilibrium where a one-electron electrochemical step is followed by another one-electron electrochemical rate-determining step.[71, 75] Typically, Tafel slopes close to 40 mV dec^{-1} are indicative of a second-electron transfer step as the rate determining step.[76-77] In comparison, a Tafel slope value of 60 mV dec^{-1} occurs when the rate-determining step involves a chemical step after the first electron transfer step.[78] Judging by the Tafel slope values for the three nanoparticles, there arises a distinct possibility that the OER kinetics for $Fe_{50}Ni_{50}$ and $Fe_{80}Ni_{20}$ was controlled by second-electron transfer step as the rate determining step and the kinetics for $Fe_{20}Ni_{80}$ controlled by the chemical step following the first electron transfer step. In their work on electrodeposited nickel-iron alloy thin films, Singh et al. calculated Tafel slopes for thin films with a differing composition of iron and nickel at 40 ± 5 mV dec^{-1}. Singh et al. proposed the reaction order to be approximately 2 concerning OH^- concentration. Singh et al. also suggested that OER initiates at the Ni^{3+} sites in the mixed iron-nickel films and goes through a fast electrochemical step where surface adsorbed OH^- is formed and followed by a slow step, where desorption takes place.[79] Lyons et al. measured the Tafel slope value of around 40 mV dec^{-1} for both nickel oxide and iron oxide electrodes in their work. Lyons et al. proposed that the rate determining step is caused by the

formation of an -OOH species for iron oxides, while the mechanism for nickel oxides was similar to that of iron oxides.[78]

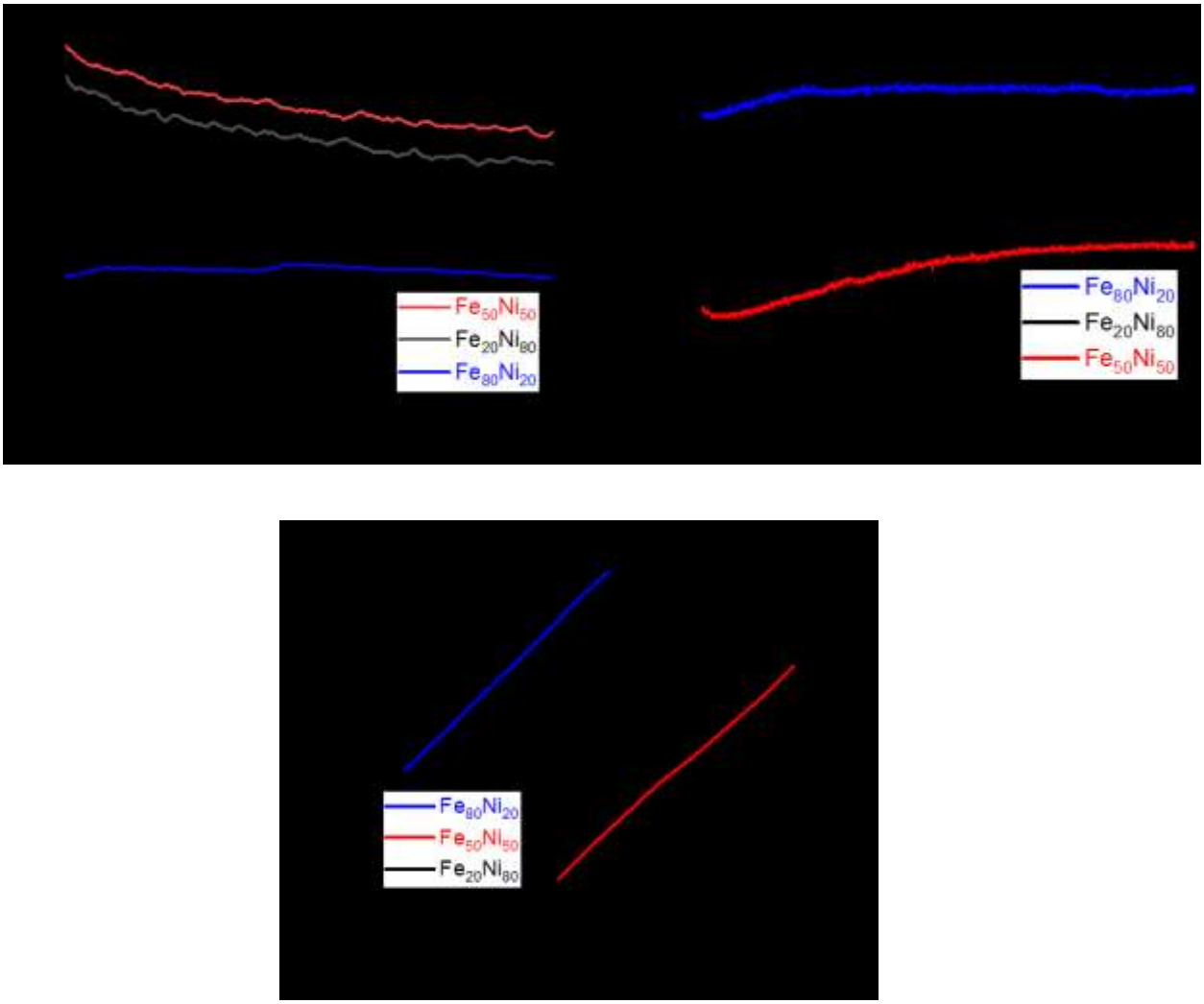

Figure 5. (a) Chronoamperometry of Fe-Ni NPs at 1.6V vs. RHE. (b) Chronopotentiometry of Fe-Ni NPs at 10 mA/cm^2. (c) Tafel slopes of Fe-Ni NPs.

Table 2. Electrochemical performance of the catalysts for OER.

Sample	Tafel Slope ($mVdec^{-1}$)	Current density @ overpotential of 300mV ($mAcm^{-2}$)	Overpotential @ current density of 10 $mAcm^{-2}$ (mV)	Degradation rate	
				mA/hr	mV/hr
$Fe_{80}Ni_{20}$	48.6	0.45	363	-0.003	0.017
$Fe_{50}Ni_{50}$	44.2	3.21	326	-0.025	0.951
$Fe_{20}Ni_{80}$	62.5	5.53	313	-0.026	1.288

CONCLUSIONS

Three nanoparticles with varying iron to nickel ratios were synthesized to test whether the ratio between iron and nickel in these catalysts impacted the OER activity and performance. TEM, ICP, and EDX were used to observe the morphology and verify the composition of the nanoparticles. Characterization tools such as XPS and XANES helped in exploring and understanding the catalysts at the atomic level. Existence of different phases was found in the catalysts with iron mostly in +3 oxidation state and nickel primarily in +2 oxidation state. Electrochemistry tests (CV, CA, and CP) were performed to assess the activity and stability of the synthesized catalysts. $Fe_{20}Ni_{80}$ showed the best performance with lower overpotential and higher current density, thus indicating that bimetallic iron-nickel nanoparticles with iron around 20% and nickel 80% are the most active one. However, the stability of $Fe_{20}Ni_{80}$ underperformed compared to the other two catalysts, $Fe_{50}Ni_{50}$ and $Fe_{80}Ni_{20}$. The results of this study indicate that there is a

trend with catalysts containing a lower amount of iron having greater OER activity. However, stability is also a critical factor in the design of a catalyst and the nanoparticle with the higher iron content ($Fe_{80}Ni_{20}$) was much more stable compared to the low iron ones ($Fe_{50}Ni_{50}$ and $Fe_{20}Ni_{80}$). Thus, future research into bimetallic iron-nickel based catalysts should help in a further understanding of the effects that ratio plays in the electrocatalysis of OER to ultimately design low-cost and effective OER catalysts.

ASSOCIATED CONTENT

Supporting Information

TEM of Fe-Ni nanoparticles, EDX results of Fe-Ni nanoparticles, ICP results of Fe-Ni nanoparticles, XPS survey spectra and detailed compositional results, XANES and EXAFS spectra for Fe-Ni nanoparticles and relevant standards

AUTHOR INFORMATION

Corresponding Author

***E-mail:** greenlee@uark.edu

ORCID

Lauren F. Greenlee: 0000-0001-6147-1533

Notes

The authors declare no competing financial interest.

ACKNOWLEDGMENTS

LFG, PA, JC, and RHM acknowledge support from the National Science Foundation, Award Number 1703827. LFG and PA acknowledge support from the National Science Foundation, Award Number 1738165. SIPB and LFG acknowledge support from the Department of Energy, Basic Energy Sciences Catalysis Program, Award # DE-SC0016529. SIPB contributed his expertise on XPS analysis for this paper. MA acknowledges support from the National Institute of Standards and Technology Phase II SBIR program and industrial collaborator AxNano, LLC through award # 100937. We thank 12BM-B at the Advanced Photon Source at Argonne National Laboratory which is supported by the U. S. Department of Energy, Office of Science, Office of Basic Energy Sciences, Scientific User Facilities Division, under the contract No. DE-AC02-06CH11357.

REFERENCES

1. Hoffert, M. I.; Caldeira, K.; Benford, G.; Criswell, D. R.; Green, C.; Herzog, H.; Jain, A. K.; Kheshgi, H. S.; Lackner, K. S.; Lewis, J. S., Advanced technology paths to global climate stability: energy for a greenhouse planet. *Science* **2002,** *298* (5595), 981-987.

2. Hoel, M.; Kverndokk, S., Depletion of fossil fuels and the impacts of global warming. *Resour. Energy Econ.* **1996,** *18* (2), 115-136.

3. Andres, R. J.; Boden, T. A.; Marland, G. *Annual Fossil-Fuel CO2 Emissions: Isomass of Emissions Gridded by One Degree Latitude by One Degree Longitude*; Carbon Dioxide Information Analysis Center (CDIAC), Oak Ridge National Laboratory (ORNL), Oak Ridge, TN (USA): 2016.

4. Steinberg, M., Fossil fuel decarbonization technology for mitigating global warming. *Int. J. Hydrog. Energy* **1999,** *24* (8), 771-777.

5. Wang, D.; Zhou, J.; Hu, Y.; Yang, J.; Han, N.; Li, Y.; Sham, T. K., In situ X-ray absorption near-edge structure study of advanced NiFe (OH) x electrocatalyst on carbon paper for water oxidation. *J. Phys. Chem. C* **2015,** *119* (34), 19573-19583.

6. Walter, M. G.; Warren, E. L.; McKone, J. R.; Boettcher, S. W.; Mi, Q.; Santori, E. A.; Lewis, N. S., Solar water splitting cells. *Chem. Rev.* **2010,** *110* (11), 6446-6473.

7. Pletcher, D.; Li, X., Prospects for alkaline zero gap water electrolysers for hydrogen production. *Int. J. Hydrog. Energy* **2011,** *36* (23), 15089-15104.

8. Swierk, J. R.; Klaus, S.; Trotochaud, L.; Bell, A. T.; Tilley, T. D., Electrochemical study of the energetics of the oxygen evolution reaction at nickel iron (oxy) hydroxide catalysts. *J. Phys. Chem. C* **2015,** *119* (33), 19022-19029.

9. Gong, M.; Dai, H., A mini review of NiFe-based materials as highly active oxygen evolution reaction electrocatalysts. *Nano Res.* **2015,** *8* (1), 23-39.

10. Hong, W. T.; Risch, M.; Stoerzinger, K. A.; Grimaud, A.; Suntivich, J.; Shao-Horn, Y., Toward the rational design of non-precious transition metal oxides for oxygen electrocatalysis. *Energy Environ. Sci.* **2015,** *8* (5), 1404-1427.

11. Morales-Guio, C. G.; Mayer, M. T.; Yella, A.; Tilley, S. D.; Grätzel, M.; Hu, X., An optically transparent iron nickel oxide catalyst for solar water splitting. *J. Am. Chem. Soc.* **2015,** *137* (31), 9927-9936.

12. Gao, Y.; Li, H.; Yang, G., Amorphous Nickel Hydroxide Nanosheets with Ultrahigh Activity and Super-Long-Term Cycle Stability as Advanced Water Oxidation Catalysts. *Cryst. Growth Des.* **2015,** *15* (9), 4475-4483.

13. Fang, W.; Liu, D.; Lu, Q.; Sun, X.; Asiri, A. M., Nickel promoted cobalt disulfide nanowire array supported on carbon cloth: an efficient and stable bifunctional electrocatalyst for full water splitting. *Electrochem. Commun.* **2016,** *63*, 60-64.

14. Jin, H.; Wang, J.; Su, D.; Wei, Z.; Pang, Z.; Wang, Y., In situ cobalt–cobalt oxide/N-doped carbon hybrids as superior bifunctional electrocatalysts for hydrogen and oxygen evolution. *J. Am. Chem. Soc.* **2015,** *137* (7), 2688-2694.

15. Kanan, M. W.; Nocera, D. G., In situ formation of an oxygen-evolving catalyst in neutral water containing phosphate and Co2+. *Science* **2008,** *321* (5892), 1072-1075.

16. Concepcion, J. J.; Jurss, J. W.; Brennaman, M. K.; Hoertz, P. G.; Patrocinio, A. O. T.; Murakami Iha, N. Y.; Templeton, J. L.; Meyer, T. J., Making oxygen with ruthenium complexes. *Acc. Chem. Res.* **2009,** *42* (12), 1954-1965.

17. Yang, Y.; Zhou, M.; Guo, W.; Cui, X.; Li, Y.; Liu, F.; Xiao, P.; Zhang, Y., NiCoO2 nanowires grown on carbon fiber paper for highly efficient water oxidation. *Electrochim. Acta* **2015,** *174*, 246-253.

18. Lee, Y.; Suntivich, J.; May, K. J.; Perry, E. E.; Shao-Horn, Y., Synthesis and activities of rutile IrO2 and RuO2 nanoparticles for oxygen evolution in acid and alkaline solutions. *J. Phys. Chem. Lett.* **2012,** *3* (3), 399-404.

19. Zhu, X.; Tang, C.; Wang, H. F.; Zhang, Q.; Yang, C.; Wei, F., Dual-sized NiFe layered double hydroxides in situ grown on oxygen-decorated self-dispersal nanocarbon as enhanced water oxidation catalysts. *J. Mater. Chem. A* **2015,** *3* (48), 24540-24546.

20. Burke, M. S.; Kast, M. G.; Trotochaud, L.; Smith, A. M.; Boettcher, S. W., Cobalt–iron (oxy) hydroxide oxygen evolution electrocatalysts: the role of structure and composition on activity, stability, and mechanism. *J. Am. Chem. Soc.* **2015,** *137* (10), 3638-3648.

21. Tang, C.; Wang, H. F.; Wang, H. S.; Wei, F.; Zhang, Q., Guest–host modulation of multi-metallic (oxy) hydroxides for superb water oxidation. *J. Mater. Chem. A* **2016,** *4* (9), 3210-3216.

22. Merrill, M. D.; Dougherty, R. C., Metal oxide catalysts for the evolution of O2 from H2O. *J. Phys. Chem. C* **2008,** *112* (10), 3655-3666.

23. Bates, M. K.; Jia, Q.; Doan, H.; Liang, W.; Mukerjee, S., Charge-transfer effects in Ni–Fe and Ni–Fe–Co mixed-metal oxides for the alkaline oxygen evolution reaction. *ACS Catal.* **2015,** *6* (1), 155-161.

24. Trotochaud, L.; Boettcher, S. W., Precise oxygen evolution catalysts: Status and opportunities. *Scr. Mater.* **2014,** *74*, 25-32.

25. Klaus, S.; Louie, M. W.; Trotochaud, L.; Bell, A. T., Role of Catalyst Preparation on the Electrocatalytic Activity of Ni1–x Fe x OOH for the Oxygen Evolution Reaction. *J. Phys. Chem. C* **2015,** *119* (32), 18303-18316.

26. Corrigan, D. A., The catalysis of the oxygen evolution reaction by iron impurities in thin film nickel oxide electrodes. *J. Electrochem. Soc.* **1987,** *134* (2), 377-384.

27. Shinagawa, T.; Garcia-Esparza, A. T.; Takanabe, K., Insight on Tafel slopes from a microkinetic analysis of aqueous electrocatalysis for energy conversion. *Sci. Rep.* **2015,** *5*, 13801.

28. Friebel, D.; Louie, M. W.; Bajdich, M.; Sanwald, K. E.; Cai, Y.; Wise, A. M.; Cheng, M. J.; Sokaras, D.; Weng, T. C.; Alonso-Mori, R., Identification of highly active Fe sites in (Ni, Fe) OOH for electrocatalytic water splitting. *J. Am. Chem. Soc.* **2015,** *137* (3), 1305-1313.

29. Stevens, M. B.; Trang, C. D. M.; Enman, L. J.; Deng, J.; Boettcher, S. W., Reactive Fe-sites in Ni/Fe (oxy) hydroxide are responsible for exceptional oxygen electrocatalysis activity. *J. Am. Chem. Soc.* **2017,** *139* (33), 11361-11364.

30. Louie, M. W.; Bell, A. T., An investigation of thin-film Ni–Fe oxide catalysts for the electrochemical evolution of oxygen. *J. Am. Chem. Soc.* **2013,** *135* (33), 12329-12337.

31. Trotochaud, L.; Young, S. L.; Ranney, J. K.; Boettcher, S. W., Nickel–iron oxyhydroxide oxygen-evolution electrocatalysts: the role of intentional and incidental iron incorporation. *J. Am. Chem. Soc.* **2014,** *136* (18), 6744-6753.

32. Steimecke, M.; Seiffarth, G.; Bron, M., In situ characterization of Ni and Ni/Fe thin film electrodes for oxygen evolution in alkaline media by a Raman-coupled scanning electrochemical microscope setup. *Anal. Chem.* **2017,** *89* (20), 10679-10686.

33. Fidelsky, V.; Toroker, M. C., The secret behind the success of doping nickel oxyhydroxide with iron. *Phys. Chem. Chem. Phys.* **2017,** *19* (11), 7491-7497.

34. Elbaz, Y.; Caspary Toroker, M., Dual Mechanisms: Hydrogen Transfer during Water Oxidation Catalysis of Pure and Fe-Doped Nickel Oxyhydroxide. *J. Phys. Chem. C* **2017,** *121* (31), 16819-16824.

35. Doyle, A. D.; Bajdich, M.; Vojvodic, A., Theoretical Insights to Bulk Activity Towards Oxygen Evolution in Oxyhydroxides. *Catal. Lett.* **2017,** *147* (6), 1533-1539.

36. Shin, H.; Xiao, H.; Goddard, W. A., In silico discovery of new dopants for Fe-doped Ni oxyhydroxide ($Ni_{1-x}Fe_xOOH$) catalysts for oxygen evolution reaction. *J. Am. Chem. Soc.* **2018**.

37. Burke, M. S.; Enman, L. J.; Batchellor, A. S.; Zou, S.; Boettcher, S. W., Oxygen evolution reaction electrocatalysis on transition metal oxides and (oxy) hydroxides: activity trends and design principles. *Chem. Mater.* **2015,** *27* (22), 7549-7558.

38. Görlin, M.; Chernev, P.; Ferreira de Araújo, J.; Reier, T.; Dresp, S.; Paul, B.; Krähnert, R.; Dau, H.; Strasser, P., Oxygen evolution reaction dynamics, faradaic charge efficiency, and the active metal redox states of Ni–Fe oxide water splitting electrocatalysts. *J. Am. Chem. Soc.* **2016,** *138* (17), 5603-5614.

39. Liu, Z.; Yu, H.; Dong, B.; Yu, X.; Feng, L., Electrochemical oxygen evolution reaction efficiently boosted by thermal-driving core–shell structure formation in nanostructured FeNi/S, N-doped carbon hybrid catalyst. *Nanoscale* **2018,** *10* (35), 16911-16918.

40. Liu, Z.; Yu, X.; Yu, H.; Xue, H.; Feng, L., Nanostructured $FeNi_3$ Incorporated with Carbon Doped with Multiple Nonmetal Elements for the Oxygen Evolution Reaction. *ChemSusChem* **2018,** *11* (16), 2703-2709.

41. Meng, H.; Ren, Z.; Du, S.; Wu, J.; Yang, X.; Xue, Y.; Fu, H., Engineering a stereo-film of $FeNi_3$ nanosheet-covered FeOOH arrays for efficient oxygen evolution. *Nanoscale* **2018,** *10* (23), 10971-10978.

42. Du, Y.; Han, Y.; Huai, X.; Liu, Y.; Wu, C.; Yang, Y.; Wang, L., N-doped carbon coated FeNiP nanoparticles based hollow microboxes for overall water splitting in alkaline medium. *Int. J. Hydrog. Energy* **2018,** *43* (49), 22226-22234.

43. Li, M.; Li, H.; Xu, T.; Nie, Y., Synthesis, Characterization and Electromagnetic Properties of SnO-coated FeNi Alloy Nanocapsules. *Mater. Res.* **2016,** *19* (6), 1393-1398.

44. Ding, X.; Huang, Y.; Wang, J., Synthesis of $FeNi_3$ nanocrystals encapsulated in carbon nanospheres/reduced graphene oxide as a light weight electromagnetic wave absorbent. *RSC Adv.* **2015,** *5* (80), 64878-64885.

45. Xia, Z.; He, J.; Ou, X.; He, S.; Zhao, D.; Yu, G., Influence of electric field on the microstructures and magnetic softness of FeNi nanoparticle films. *Appl. Phys. A* **2016,** *122* (9), 860.

46. Greenlee, L. F.; Rentz, N. S., ATMP-stabilized iron nanoparticles: chelator-controlled nanoparticle synthesis. *J. Nanoparticle Res.* **2014,** *16* (11), 2712.

47. Gilbert, J. B.; Rubner, M. F.; Cohen, R. E., Depth-profiling X-ray photoelectron spectroscopy (XPS) analysis of interlayer diffusion in polyelectrolyte multilayers. *Proc. Natl. Acad. Sci. U.S.A.* **2013**, 201222325.

48. Candelaria, S. L.; Bedford, N. M.; Woehl, T. J.; Rentz, N. S.; Showalter, A. R.; Pylypenko, S.; Bunker, B. A.; Lee, S.; Reinhart, B.; Ren, Y., Multi-component Fe–Ni hydroxide nanocatalyst for oxygen evolution and methanol oxidation reactions under alkaline conditions. *ACS Catal.* **2016,** *7* (1), 365-379.

49. Grosvenor, A. P.; Kobe, B. A.; Biesinger, M. C.; McIntyre, N. S., Investigation of multiplet splitting of Fe 2p XPS spectra and bonding in iron compounds. *Surf. Interface Anal.* **2004,** *36* (12), 1564-1574.

50. McIntyre, N. S.; Zetaruk, D. G., X-ray photoelectron spectroscopic studies of iron oxides. *Anal. Chem.* **1977,** *49* (11), 1521-1529.

51. Temesghen, W.; Sherwood, P., Analytical utility of valence band X-ray photoelectron spectroscopy of iron and its oxides, with spectral interpretation by cluster and band structure calculations. *Anal. Bioanal. Chem.* **2002,** *373* (7), 601-608.

52. Grosvenor, A. P.; Biesinger, M. C.; Smart, R.; McIntyre, N. S., New interpretations of XPS spectra of nickel metal and oxides. *Surf. Sci.* **2006,** *600* (9), 1771-1779.

53. Biesinger, M. C.; Payne, B. P.; Lau, L. W. M.; Gerson, A.; Smart, R., X-ray photoelectron spectroscopic chemical state quantification of mixed nickel metal, oxide and hydroxide systems. *Surf. Interface Anal.* **2009,** *41* (4), 324-332.

54. Balasubramanian, C.; Joseph, B.; Gupta, P.; Saini, N. L.; Mukherjee, S.; Di Gioacchino, D.; Marcelli, A., X-ray absorption spectroscopy characterization of iron-oxide nanoparticles synthesized by high temperature plasma processing. *J. Electron. Spectrosc. Relat. Phenom* **2014,** *196*, 125-129.

55. Manceau, A.; Gates, W. P., Surface structural model for ferrihydrite. *Clays Clay Miner* **1997,** *45* (3), 448-460.

56. Berry, A. J.; O'Neill, H.; Jayasuriya, K. D.; Campbell, S. J.; Foran, G. J., XANES calibrations for the oxidation state of iron in a silicate glass. *Am. Mineral.* **2003,** *88* (7), 967-977.

57. Kim, S.; Tryk, D. A.; Antonio, M. R.; Carr, R.; Scherson, D., In situ X-ray absorption fine structure studies of foreign metal ions in nickel hydrous oxide electrodes in alkaline electrolytes. *J. Phys. Chem.* **1994,** *98* (40), 10269-10276.

58. Wang, W.; Ding, Z.; Zhao, X.; Wu, S.; Li, F.; Yue, M.; Liu, J. P., Microstructure and magnetic properties of MFe2O4 (M= Co, Ni, and Mn) ferrite nanocrystals prepared using colloid mill and hydrothermal method. *J. Appl. Phys.* **2015,** *117* (17), 17A328.

59. Boubnov, A.; Lichtenberg, H.; Mangold, S.; Grunwaldt, J. D., Identification of the iron oxidation state and coordination geometry in iron oxide-and zeolite-based catalysts using pre-edge XAS analysis. *J. Synchrotron Radiat.* **2015,** *22* (2), 410-426.

60. McKeehan, L. W., The Crystal Structure of Iron-Nickel Alloys. *Phys. Rev.* **1923,** *21* (4), 402.

61. Jeevanandam, P.; Koltypin, Y.; Gedanken, A., Synthesis of nanosized α-nickel hydroxide by a sonochemical method. *Nano Lett.* **2001,** *1* (5), 263-266.

62. Hall, D. S.; Lockwood, D. J.; Bock, C.; MacDougall, B. R., Nickel hydroxides and related materials: a review of their structures, synthesis and properties. *Proc. R. Soc. A* **2015,** *471* (2174), 20140792.

63. McBreen, J.; O'Grady, W. E.; Tourillon, G.; Dartyge, E.; Fontaine, A.; Pandya, K. I., In situ time-resolved x-ray absorption near edge structure study of the nickel oxide electrode. *J. Phys. Chem.* **1989,** *93* (17), 6308-6311.

64. Mansour, A. N.; Melendres, C. A.; Pankuch, M.; Brizzolara, R. A., X-Ray Absorption Fine Structure Spectra and the Oxidation State of Nickel in Some of Its Oxycompounds. *J. Electrochem. Soc.* **1994,** *141* (6), L69-L71.

65. Motori, A.; Sandrolini, F.; Davolio, G., Electrical properties of nickel hydroxide for alkaline cell systems. *J. Power Sources* **1994,** *48* (3), 361-370.

66. Cheng, C., Enhanced magnetization and conductive phase in NiFe2O4. *J. Magn. Magn. Mater.* **2013,** *325*, 144-146.

67. Bediako, D. K.; Lassalle-Kaiser, B.; Surendranath, Y.; Yano, J.; Yachandra, V. K.; Nocera, D. G., Structure–activity correlations in a nickel–borate oxygen evolution catalyst. *J. Am. Chem. Soc.* **2012,** *134* (15), 6801-6809.

68. Pandya, K. I.; Hoffman, R. W.; McBreen, J.; O'Grady, W. E., In situ X-ray absorption spectroscopic studies of nickel oxide electrodes. *J. Electrochem. Soc.* **1990,** *137* (2), 383-388.

69. Speck, F. D.; Dettelbach, K. E.; Sherbo, R. S.; Salvatore, D. A.; Huang, A.; Berlinguette, C. P., On the electrolytic stability of iron-nickel oxides. *Chem* **2017,** *2* (4), 590-597.

70. Acharya, P.; Burrow, J.; Abolhassani, M.; Greenlee, L. F., Role of Surface Area on the Performance of Iron Nickel Nanoparticles for the Oxygen Evolution Reaction (OER). *ECS Transactions* **2018,** *85* (11), 81-89.

71. Lu, Z.; Xu, W.; Zhu, W.; Yang, Q.; Lei, X.; Liu, J.; Li, Y.; Sun, X.; Duan, X., Three-dimensional NiFe layered double hydroxide film for high-efficiency oxygen evolution reaction. *ChemComm* **2014,** *50* (49), 6479-6482.

72. Hu, C. C.; Wu, Y. R., Bipolar performance of the electroplated iron–nickel deposits for water electrolysis. *Mater. Chem. Phys.* **2003,** *82* (3), 588-596.

73. Li, X.; Walsh, F. C.; Pletcher, D., Nickel based electrocatalysts for oxygen evolution in high current density, alkaline water electrolysers. *Phys. Chem. Chem. Phys.* **2011,** *13* (3), 1162-1167.

74. Görlin, M.; Ferreira de Araújo, J.; Schmies, H.; Bernsmeier, D.; Dresp, S.; Gliech, M.; Jusys, Z.; Chernev, P.; Kraehnert, R.; Dau, H., Tracking catalyst redox states and reaction dynamics in Ni–Fe oxyhydroxide oxygen evolution reaction electrocatalysts: The role of catalyst support and electrolyte pH. *J. Am. Chem. Soc.* **2017,** *139* (5), 2070-2082.

75. Castro, E. B.; Gervasi, C. A., Electrodeposited Ni–Co-oxide electrodes: characterization and kinetics of the oxygen evolution reaction. *Int. J. Hydrog. Energy* **2000,** *25* (12), 1163-1170.

76. Giménez, S.; Bisquert, J., *Photoelectrochemical solar fuel production*. Springer: 2016.

77. Marshall, A. T.; Vaisson-Béthune, L., Avoid the quasi-equilibrium assumption when evaluating the electrocatalytic oxygen evolution reaction mechanism by Tafel slope analysis. *Electrochem. Commun.* **2015,** *61*, 23-26.

78. Lyons, M. E. G.; Brandon, M. P., A comparative study of the oxygen evolution reaction on oxidised nickel, cobalt and iron electrodes in base. *J. Electroanal. Chem.* **2010,** *641* (1-2), 119-130.

79. Singh, R. N.; Pandey, J. P.; Anitha, K. L., Preparation of electrodeposited thin films of Nickel-Iron alloys on mild steel for alkaline water electrolysis. Part I: Studies on oxygen evolution. *Int. J. Hydrog. Energy* **1993,** *18* (6), 467-473.

For Table of Contents Only